**Article:**
Wang, K, Zhou, J, Ma, Y et al. (2 more authors) (2023) Constitutive and numerical modeling for the coupled thermal-hydro-mechanical processes in dual-porosity geothermal reservoir. Applied Thermal Engineering, 223. 120027. ISSN 1359-4311

https://doi.org/10.1016/j.applthermaleng.2023.120027

# Constitutive and numerical modeling for the coupled thermal-hydro-mechanical processes in dual-porosity geothermal reservoir

Kai WANG[1,2], Jiahui ZHOU[2], Yue MA[2]*, Aizhong DING[1], Xiaohui CHEN[2]

[1]College of Water Sciences, Beijing Normal University, Beijing, 100875, CHINA

[2]School of Civil Engineering, University of Leeds, Leeds, LS2 9JT, UK

*Correspondence to: Yue MA, School of Civil Engineering, University of Leeds, LS2 9JT, UK

E-mail: cnym@leeds.ac.uk

# Abstract

Enhanced geothermal system (EGS) is viewed as one of the most practical methods to explore geothermal energy in hot dry rock (HDR), which can contribute to zero carbon emissions and provide reliable and renewable energy. Modelling the performance and long-term environmental effects of the EGS remains a challenge as the rock is often fractured and experiences complicated multi-physics coupling behaviour. Despite studies on constitutive or numerical modelling of coupled behaviour in deformable dual-porosity media, those developed models often ignore the fully coupled processes in heat transfer and are highly empirical. Based on a non-equilibrium thermodynamics approach, the Mixture-Coupling Theory, this research derives the fully coupled Thermo-Hydro-Mechanical (THM) governing equations for dual-porosity geothermal reservoirs, addressing the interaction between strain, pore/fracture pressure and temperature. The constitutive model is obtained by the analysis of Helmholtz free energy evolution in dual-porosity reservoirs. The proposed model determines the fully coupled evolution of solid stress, both pore and fracture porosity, and solid entropy density. The governing equations can predict the fully coupled THM effect in dual-porosity geothermal reservoirs. Numerical modelling is then performed to study the production performance and coupled THM response in an EGS. The modelling results show that the production temperature is determined by the coupled THM effects. Porosity change is mainly determined by temperature change (accounting for over 87% of the total porosity change) during the extraction. The porosity change accounts for 1.03% and 1.23% of the initial porosity for pore and fracture, separately.



Keywords: Dual porosity, Thermal-Hydraulic-Mechanical, Hot dry rock, non-equilibrium thermodynamics

# 1. Introduction

Under the background of changing climate, a comprehensive consideration of the heat transfer in the subsurface and its interaction with fluid flow and soil or rock becomes more and more important in thermal energy exploitation and application (Dahash et al., 2021; Zhou et al., 2013), and construction in temperature sensitive areas(Chen et al., 2021a; Chen et al., 2021b). In recent years, to achieve zero carbon emissions, Hot dry rock (HDR) geothermal energy, as an easily obtainable renewable energy source from earth crystalline formations, is raising the attention of many researchers (Aliyu and Archer, 2021b; Houhou and Laloui, 2022; Wang et al., 2021). HDR exploitation, also referred to as the enhanced geothermal system (EGS), is first developed by researchers from the US (Tester et al., 2007). Cold water is pumped into the HDR reservoir through injection wells and is heated when flowing through the reservoir. Hot water can then be produced through the production well and be used as a renewable energy source which contributes to carbon reduction (Chen and Jiang, 2015).

Since the permeability of natural HDR is very low, fracturing technology is used to create new fractures within the rock, which transforms the HDR into fractured porous media. So, modelling the performance of the HDR extraction system is a challenging work as it requires a proper conceptual model to address the feature of the fracture network or the matrix in the reservoir. Different conceptual methods have been developed, including equivalent continuum models (Dykhuizen, 1990; Li et al., 2020; Saevik et al., 2013; Shu, 1999), discrete fracture models (Jiang and Younis, 2017; Lee et al., 2001) and the dual-porosity theory (Aifantis, 1980; Barenblatt et al., 1960; Warren and Root, 1963). The dual-porosity theory gives an important assumption that fractured porous media is formed as two overlapping domains, the pore matrix and the fracture, they are both continua but with different hydraulic and mechanical characteristics (Barenblatt et al., 1960; Warren and Root, 1963). In addition, the water and energy exchanges between the fracture and pore matrix due to the gradient of water pressure and temperature. Dual-porosity theory has been applied in geotechnics and environmental field (Gelet et al., 2012b; Hosking et al., 2020; Leij et al., 2012; Zhang and Cui, 2011), which shows a potential advantage in achieving a balance in model simplification and calculation precision on both fracture and pore matrix.

Based on the dual-porosity concept, some research works have been conducted to explore the behaviour of mechanical, hydraulic, and thermal processes in fractured media. For example, Bai and Roegiers (1994) developed the very early coupled THM constitutive model for dual-porosity media; Masters et al. (2000) proposed a coupled THM model, which assumes a single representative thermodynamics continuum including both heat conduction and convection. Zhang and Cui (2011) developed a THM model, in which the thermal effect on the hydraulic field is ignored. Khalili and Selvadurai (2003) presented a fully coupled THM constitutive model using a systematic macroscopic way; while the above studies are based on the mechanics approach, Gelet et al. (2012b) derived a THM model through a thermodynamics way.

Apart from the constitutive work, some numerical simulations were done. Aliyu and Archer (2021b); Aliyu and Chen (2017); Sun et al. (2017) used 3D numerical models to investigate the responses of thermal productivity on the variation of human control parameters. Sun et al. (2018) studied the optimizations of EGS heat extraction to improve the thermal extraction capacity, according to the THM numerical prediction. Li et al. (2018) studied the effects of Local thermal non-equilibrium (LTNE) on solid deformation based on semi-analytical solutions and numerical models. Taron and Elsworth (2009) compared permeability and porosity change between injection and withdrawal well, which is induced by different mechanisms. Rutqvist et al. (2009) evaluated the variation of permeability and its effect on the fluid flow around the reservoir. Zhao et al. (2015) used THM coupled model of fractured media to simulate the extraction of geothermal energy based on a geothermal field in Tengchong, China. However, the above mentioned numerical works often use constant porosity values in the modelling, despite the fact that porosity changes with temperature/pressure/deformation and affect the distribution of pressure/deformation in turn (Wang et al., 2022). Therefore, the porosity as a time dependent variable, and its application in the numerical modeling (i.e., using dynamic porosity in modelling) is essential to give a better behaviour prediction of the HDR reservoir and EGS.

At present, most of the existing coupled thermal-hydro-mechanical constitutive equations are not presented in a fully coupled way, especially for the thermal equation which usually ignores the impact of the strain (mechanical) and pressure (hydro) processes, making it decoupled from the mechanical and hydro fields. This mainly results from two reasons. One is that many researchers consider the strain and pressure influence on the thermal process is not significant, especially when the porosity change due to strain and pressure is limited, therefore the thermal

equation omits the strain and pressure terms. Another reason can be attributed to the approach that was adopted to develop the equations. Most of the THM constitutive models are developed by the mechanics approach, which forms the constitutive relationships by directly analysing the stress-strain relationship through continuum mechanics. Therefore, these models are highly empirical and rely on the intuition of the researcher.

Considering the increasing need for HDR modelling and challenges in mathematical THM model development, this research develops new governing equations of thermo-hydro-mechanical coupled behaviour in dual-porosity media based on a non-equilibrium thermodynamics approach, the Mixture-Coupling Theory (Chen et al., 2016; Heidug and Wong, 1996; Ma et al., 2022). The multi-physical constitutive model is derived from the analysis of Helmholtz free energy change in the dual-porosity media. The whole derivation is thermodynamics-consistent. The presented equations successfully determine the THM coupled effects in deformable dual-porosity media including the fluid-induced and heat-induced deformation, and porosity evolution which is caused by the solid strain, the pore and fracture fluid pressure, and the temperature change. Then a finite element numerical case is used to study the multi-physics response during the production of the enhanced geothermal system and to compare with a baseline model.

## 2. Balance equation

Thermal, hydro, and mechanical fields are coupled in the HDR, and the study of hydro-mechanical effects on the thermal transport and vice versa can help answer how the coupling (such as the water flow, rock deformation and porosity change) affects the heat transfer or production efficiency. Let us consider a Representative Elementary Volume (REV) in a dual-porosity HDR, with fluid flow in both porous matrix and fracture. The REV is a mixture of solids and liquids with a volume $V$ and boundary $S$ attached to the solid phase, there is no movement of solids across the domain boundary; only movement of fluid. There is thermal transport caused by a temperature gradient within the REV, which influences all components (e.g. water and solid). The derivation of the basic balance equation for energy and mass in this REV is illustrated below.

If $\beta = (Mf, Ff)$ represent the matrix pore fluid $Mf$ and fracture fluid $Ff$ . The volume fraction of the matrix pore and fracture is defined as

$$\phi^{\beta} = \frac{V^{\beta}}{V} \tag{1}$$

where $V^{\beta}$ is the volume of the matrix pore space and the fracture space. The paper considers the saturated case, therefore, $V^{\beta}$ also represents the volume of matrix pore fluid and fracture fluid. The volume fraction must obey $\sum \phi^{\beta} = 1 - \phi^{s}$, where $\phi^{s}$ is the volume fraction of the solid.

The mass density can be defined in two different ways: (1) the mixture mass density $\rho^{\beta}$ based on the volume of the whole mixture; or (2) the density $\rho_{\beta}^{\beta}$ based on the volume of the constituent volume $V^{\beta}$. The density relationship obeys

$$\rho^{\beta} = \phi^{\beta} \rho_{\beta}^{\beta} \tag{2}$$

### 2.1 Fluid mass balance equation

The fracture and the matrix pore space are assumed to be saturated by the same kind of fluids, so the mass balance equations for the two regions should involve not only the flux leaving the region, but also the fluid exchange between the matrix pore and the fracture. Therefore, the balance equation for fluid mass is

$$\frac{D}{Dt}\left(\int_{V} \rho^{\beta} dV\right) = -\int_{S} \mathbf{I}^{\beta} \cdot \mathbf{n} dS - \int_{V} \tilde{\rho}^{\beta} dV \tag{3}$$

in which $\tilde{\rho}^{\beta}$ is the fluid mass exchanging between the matrix pore and the fracture, it must satisfy the close relationship $\sum \tilde{\rho}^{\beta} = 0$ (i.e., $\tilde{\rho}^{Mf} = -\tilde{\rho}^{Ff}$). $\mathbf{I}^{\beta} = \rho^{\beta}\left(\mathbf{v}^{\beta} - \mathbf{v}^{s}\right)$ is the fluid flux; $\mathbf{v}^{\beta}$ is the interstitial velocity of fluid; $\mathbf{v}^{s}$ is the velocity of the solid phase, i.e., the rate of change of position of solid particles; $\mathbf{v}^{\beta} - \mathbf{v}^{s}$ means the relative velocity of fluid (Biot, 1956); $\mathbf{n}$ is the outward unit normal vector.

The time derivative following the motion of the solid is $\frac{d(\cdot)}{dt} = \frac{\partial(\cdot)}{\partial t} + \mathbf{v}^{s} \cdot \nabla(\cdot)$, where $\nabla$ is the gradient. Then, the mass balance equation (3) in local form can be written as

$$\dot{\rho}^{\beta} + \rho^{\beta} \nabla \cdot \mathbf{v}^{s} + \nabla \cdot \mathbf{I}^{\beta} + \tilde{\rho}^{\beta} = 0 \tag{4}$$

### 2.2 Entropy balance equation

The fluid transporting through the matrix pore or the fracture is an irreversible process, the entropy change during this process combines two parts: the entropy exchange with surroundings $\mathbf{I}_\eta$ and the entropy produced irreversibly $\gamma$. The entropy balance equation for the mixture can be written as (Katchalsky and Curran, 1965)

$$\dot{\eta}^{mix} + \eta^{mix}\nabla\cdot\mathbf{v}^s + \nabla\cdot\mathbf{I}_\eta - \gamma = 0 \tag{5}$$

where $\eta^{mix}$ is the entropy of the mixture, including the entropy of the solid and the fluids.

The entropy exchange with surroundings $\mathbf{I}_\eta$ written as

$$\mathbf{I}_\eta = \frac{\mathbf{q} - \sum \mu^\beta \mathbf{I}^\beta}{T} = \frac{\mathbf{q}'}{T} + \sum \eta^\beta \mathbf{I}^\beta \tag{6}$$

where $T$ is temperature; $\mu^\beta = h^\beta - T\eta^\beta$ is the chemical potential of fluid $\beta$, $h^\beta$ is the enthalpy; $\mathbf{q}$ is the total heat flow, which can be divided into two parts: (1) the reduced heat flow $\mathbf{q}'$, which is the heat exchange through the direct contact on the boundary with the surrounding; (2) the heat flow carried by fluid through convection $\sum h^\beta \mathbf{I}^\beta$.

### 2.3 Helmholtz Free Energy balance equation

The Helmholtz free energy of the mixture $\psi$ is defined as the difference between the internal energy of the mixture $\varepsilon^{mix}$ and the contribution of entropy $T\eta$

$$\psi = \varepsilon^{mix} - T\eta^{mix} \tag{7}$$

Then, the derivative of free energy density following the motion of the solid is

$$\dot{\psi} + \psi\nabla\cdot\mathbf{v}^s = \dot{\varepsilon}^{mix} + \varepsilon^{mix}\nabla\cdot\mathbf{v}^s - \left(\dot{T} + T\nabla\cdot\mathbf{v}^s\right)\eta^{mix} - T\left(\dot{\eta}^{mix} + \eta^{mix}\nabla\cdot\mathbf{v}^s\right) \tag{8}$$

The internal energy balance equation can be written as (Ma et al., 2022)

$$\dot{\varepsilon}^{mix} + \varepsilon^{mix}\nabla\cdot\mathbf{v}^s - \nabla\cdot\left(\boldsymbol{\sigma}\mathbf{v}^s\right) + \nabla\cdot\mathbf{q}' + \nabla\cdot\sum h^\beta \mathbf{I}^\beta = 0 \tag{9}$$

where $\boldsymbol{\sigma}$ is the Cauchy stress tensor.

Therefore, based on equation (8), with equation (9) and (5), the Helmholtz free energy density of the mixture can be obtained as

$$\dot{\psi}+\psi\nabla\cdot\mathbf{v}^{s}=\nabla\cdot\left(\boldsymbol{\sigma}\mathbf{v}^{s}\right)-\nabla\cdot\mathbf{q}'-\nabla\cdot\sum h^{\beta}\mathbf{I}^{\beta}-\left(\dot{T}+T\nabla\cdot\mathbf{v}^{s}\right)\eta^{mix}+T\nabla\cdot\mathbf{I}_{\eta}-T\gamma \tag{10}$$

# 3. Entropy product and transport law

## 3.1 Entropy production

The entropy production in the mixture system involves three parts: 1. the friction of matrix pore fluid transport $\vartheta_{Mf}$, the fraction of fracture fluid transport $\vartheta_{Ff}$; 2. the fraction generated fluid exchange between these two networks $\vartheta_{ex}$; 3. the entropy generated by thermal exchange with the surroundings $\vartheta_{th}$. From non-equilibrium thermodynamics (Katchalsky and Curran, 1965), there is

$$\vartheta_{Mf}=-\mathbf{I}^{Mf}\cdot\nabla\mu^{Mf}\ ,\ \vartheta_{Ff}=-\mathbf{I}^{Ff}\cdot\nabla\mu^{Ff}\ ,\ \vartheta_{th}=-\mathbf{I}_{\eta}\cdot\nabla T \tag{11}$$

According to Gelet et al. (2012b) and Coussy (2004), $\vartheta_{ex}$ can be expressed as (assuming fluid transport from matrix pore to fracture)

$$\vartheta_{ex}=\tilde{\rho}^{Mf}\left(\mu^{Mf}-\mu^{Ff}\right) \tag{12}$$

Therefore, the over entropy production regarding the fluid and thermos transport in the dual-porosity system is

$$0\le T\gamma=-\sum\mathbf{I}^{\beta}\cdot\nabla\mu^{\beta}-\mathbf{I}_{\eta}\cdot\nabla T+\tilde{\rho}^{Mf}\left(\mu^{Mf}-\mu^{Ff}\right) \tag{13}$$

## 3.2 Transport Law

The Darcy velocity is defined as

$$\mathbf{u}^{\beta}=\phi^{\beta}\left(\mathbf{v}^{\beta}-\mathbf{v}^{s}\right) \tag{14}$$

The transport law can be derived through the entropy production and phenomenological equation. To simply the discussion, we shall neglect the coupling between the fluid flow and

the heat flow, i.e., osmotic phenomenon, and roughly adopt the Darcy's law for the transport of matrix pore fluid and fracture fluid and the Fourier's law for the transport of heat:

$$\mathbf{u}^{\beta} = -\frac{k^{\beta}}{\nu^{\beta}}\nabla p^{\beta} \ , \ \mathbf{q}' = -\lambda \nabla T \tag{15}$$

where $k^{\beta}$, $p^{\beta}$, $\nu^{\beta}$ are the intrinsic permeability, pressure, viscosity of matrix fluid and fracture fluid; $\lambda$ is the thermal conductivity.

# 4. Constitutive equation

### 4.1 Basic equation for deformation

Assuming the material maintains mechanical equilibrium, there is $\nabla \cdot \boldsymbol{\sigma} = \mathbf{0}$. With the entropy production (13) and the entropy flux equation (6), the Helmholtz free energy balance equation (10) can be converted into

$$\dot{\psi} + \psi \nabla \cdot \mathbf{v}^{s} = \nabla \cdot \left( \boldsymbol{\sigma} \mathbf{v}^{s} \right) - \left( \dot{T} + T \nabla \cdot \mathbf{v}^{s} \right) \eta^{mix} - \tilde{\rho}^{Mf} \left( \mu^{Mf} - \mu^{Ff} \right) - \sum \mu^{\beta} \nabla \cdot \mathbf{I}^{\beta} \tag{16}$$

Using the mass balance equation (4), the final two terms in equation (16) can be converted into densities as

$$\dot{\psi} + \psi \nabla \cdot \mathbf{v}^{s} = \nabla \cdot \left( \boldsymbol{\sigma} \mathbf{v}^{s} \right) - \left( \dot{T} + T \nabla \cdot \mathbf{v}^{s} \right) \eta^{mix} + \mu^{\beta} \left( \dot{\rho}^{\beta} + \rho^{\beta} \nabla \cdot \mathbf{v}^{s} \right) \tag{17}$$

Equation (17) describes the free energy density in the current configuration, following the basic relationships in continuum mechanics (Wriggers, 2008), it can be switched into the reference configuration as (Coussy, 2004; Heidug and Wong, 1996; Ma et al., 2022)

$$\dot{\Psi} = tr\left( \mathbf{T} \dot{\mathbf{E}} \right) + \sum \mu^{\beta} \dot{m}^{\beta} - \mathrm{H}^{mix} \dot{T} \tag{18}$$

in which: $\Psi = J\psi$ is the free energy in the reference configuration, $m^{\beta} = J\rho^{\beta}$ is the mass density of fluid in the reference configuration, $\mathrm{H}^{mix} = J\eta^{mix}$ is the entropy density in the reference configuration; $\mathbf{T}$ and $\mathbf{E}$ are the second Piola-Kirchhoff stress and Green strain; $J = dV/dV_0$, where $V$, $V_0$ are the volume in the current and reference configuration; The time derivation of $J$ satisfies the Euler's formula

$$\dot{J} = J \nabla \cdot \mathbf{v}^{s} \tag{19}$$

### 4.2 Helmholtz free energy density of porous/fracture water

The fluid mass in the matrix pore and the fracture follows the classic thermodynamics, therefore, the free energy of the fluids obeys

$$\psi_\beta = -p^\beta + \rho_\beta^\beta \mu^\beta \tag{20}$$

Using the Gibbs-Duhem equation for the matrix pore fluid and the fracture fluid, it leads to

$$\dot{p}^\beta = \rho_\beta^\beta \dot{\mu}^\beta + \eta_\beta^\beta \dot{T} \tag{21}$$

Invoking equation (21) into the time derivation of equation (20), the following relationships can be obtained

$$\dot{\psi}_\beta = \dot{\rho}_\beta^\beta \mu^\beta - \eta_\beta^\beta \dot{T} \tag{22}$$

### 4.3 Free energy density of the solid matrix

The free energy of the mixture system consists of three parts: the free energy of the matrix pore fluid, the free energy of the fracture fluid and the free energy of the solid matrix. By subtracting the free energy of the matrix pore fluid and the fracture fluid from the free energy of the mixture system, the free energy of the solid matrix can be obtained.

From equation (18), (22) and using the density relationship (2), the free energy density of the solid matrix is

$$\left(\Psi - \sum \upsilon^\beta \psi_\beta\right)^{\cdot} = tr\left(\mathbf{T}\dot{\mathbf{E}}\right) + \sum p^\beta \dot{\upsilon}^\beta - \mathrm{H}^s \dot{T} \tag{23}$$

where $\upsilon^\beta = J\phi^\beta$ is the porosity of matrix pore and fracture in the reference configuration $\mathrm{H}^s = J\eta^s = J\left(\eta^{mix} - \sum \eta^\beta\right)$ is the entropy density of the solid in the reference configuration.

Define $W = \left(\Psi - \sum \upsilon^\beta \psi_\beta\right) - \sum \upsilon^\beta p^\beta$ , then from equation (23), there is

$$\dot{W} = tr\left(\mathbf{T}\dot{\mathbf{E}}\right) - \sum \upsilon^\beta \dot{p}^\beta - \mathrm{H}^s \dot{T} \tag{24}$$

Till now, we shall write the equation (24) in full form as

$$\dot{W} = tr\left(\mathbf{T}\dot{\mathbf{E}}\right) - \upsilon^{Mf} \dot{p}^{Mf} - \upsilon^{Ff} \dot{p}^{Ff} - \mathrm{H}^s \dot{T} \tag{25}$$

where $W$ is a function of $\mathbf{E}$, $p^{Mf}$, $p^{Ff}$ and $T$.

From equation (25), there must be

$$T_{ij}=\left(\frac{\partial W}{\partial E_{ij}}\right)_{p^{Mw},p^{Fw},T},\upsilon^{Mw}=-\left(\frac{\partial W}{\partial p^{Mw}}\right)_{E_{ij},p^{Fw},T},\upsilon^{Fw}=-\left(\frac{\partial W}{\partial p^{Fw}}\right)_{E_{ij},p^{Mw},T},\ \mathrm{H}^{s}=-\left(\frac{\partial W}{\partial T}\right)_{E_{ij},p^{Mw},p^{Fw}} \tag{26}$$

So that

$$\dot{W}(\mathbf{E},p^{Mw},p^{Fw})=\left(\frac{\partial W}{\partial E_{ij}}\right)_{p^{Mw},p^{Fw}}\dot{E}_{ij}+\left(\frac{\partial W}{\partial p^{Mw}}\right)_{E_{ij},p^{Fw}}\dot{p}^{Mw}+\left(\frac{\partial W}{\partial p^{Fw}}\right)_{E_{ij},p^{Mw}}\dot{p}^{Fw}+\left(\frac{\partial W}{\partial T}\right)_{E_{ij},p^{Mw},p^{Fw}}\dot{T} \tag{27}$$

Differentiating equation (26) with respect to time, with the help of equation (27), the evolution of stress $T_{ij}$, matrix pore porosity $\upsilon^{Mw}$, fracture porosity $\upsilon^{Fw}$ and entropy of the solid $\mathrm{H}^{s}$ can be obtained.

$$\dot{T}_{ij}=L_{ijkl}\dot{E}_{kl}-M_{ij}\dot{p}^{Mf}-S_{ij}\dot{p}^{Ff}-F_{ij}\dot{T} \tag{28}$$

$$\dot{\upsilon}^{Mw}=M_{ij}\dot{E}_{ij}+Q\dot{p}^{Mf}+B\dot{p}^{Ff}+C_{24}\dot{T} \tag{29}$$

$$\dot{\upsilon}^{Fw}=S_{ij}\dot{E}_{ij}+B\dot{p}^{Mf}+Z\dot{p}^{Ff}T+C_{34}\dot{T} \tag{30}$$

$$\dot{\mathrm{H}}^{s}=F_{ij}\dot{E}_{ij}+C_{42}\dot{p}^{Mf}+C_{43}\dot{p}^{Ff}+C_{44}\dot{T} \tag{31}$$

where $L_{ijkl}, M_{ij}, S_{ij}, F_{ij}, Q, B, C_{24}, Z, C_{34}, C_{42}, C_{43}, C_{44}$ are coefficients.

# 5 Coupled thermo-hydro-mechanical governing equations

## 5.1 Assumptions and simplifications

Equations (28), (29), (30) (31) are the very general coupled equations for stress, strain, matrix pore/fracture fluid pressure and matrix pore/fracture porosity, as well as temperature. Following the linear, isotropic and small strain assumption (Berryman and Wang, 1995; Heidug and Wong, 1996), the stress equation (28) and the volume fraction equation (29), (30) for the elastic deformation can be simplified as(Heidug and Wong, 1996)

$$\dot{\sigma}_{ij} = \left( K - \frac{2G}{3} \right) \dot{\varepsilon}_{kk} \delta_{ij} + 2G\dot{\varepsilon}_{ij} - \zeta^{Mf} \dot{p}^{Mf} \delta_{ij} - \zeta^{Ff} \dot{p}^{Ff} \delta_{ij} - \beta_T \dot{T} \delta_{ij} \tag{32}$$

$$\dot{\upsilon}^{Mf} = \zeta^{Mf} \dot{\varepsilon}_{ii} + Q\dot{p}^{Mf} + B\dot{p}^{Ff} + C_{24}\dot{T} \tag{33}$$

$$\dot{\upsilon}^{Ff} = \zeta^{Ff} \dot{\varepsilon}_{ii} + B\dot{p}^{Mf} + Z\dot{p}^{Ff} + C_{34}\dot{T} \tag{34}$$

where $\zeta^{Ff} = 1 - \frac{K}{K_{pb}}$, $\zeta^{Mf} = \frac{K}{K_{pb}} - \frac{K}{K_s}$ are the effective stress coefficients, with $K$, $K_{pb}$, $K_s$ being the bulk modulus of the mixture, the porous block, the solid grain, respectively; $\beta_T$ is the thermal expansion coefficient of the solid.

Equation (33) and (34) determine the matrix and fracture porosity change with solid deformation, fluid pressure and temperature, enabling us to explore the porosity evolution and set the porosity as a dynamic variable in the numerical modelling.

The parameters $Q$, $B$, $Z$ are

$$\begin{aligned} Q &= \left( \frac{1}{K_{pb}} - \frac{1}{K_s} \right) \left( 1 - \frac{K}{K_{pb}} + \frac{K}{K_s} - \phi^{Ff} \right) - \frac{\phi^{Mf}}{K_s} \\ B &= \left( 1 - \frac{K}{K_{pb}} - \phi^{Ff} \right) \left( \frac{1}{K_s} - \frac{1}{K_{pb}} \right) \\ Z &= \frac{1}{K_{pb}} \left( 1 - \frac{K}{K_{pb}} - \phi^{Ff} \right) \end{aligned} \tag{35}$$

The identification of the parameters $C_{24}$, $C_{34}$ is represented in the next section.

## 5.2 Parameter identification

*5.2.1. Identification of $C_{24}$ and $C_{34}$*

For the matrix pore, void volume change due to temperature can be written as

$$\dot{\upsilon}^{Mf} = \phi^{Mf} \beta_T \dot{T} \tag{36}$$

At equilibrium, the fluid pressure influence vanishes, e.g. $\dot{p}^{Mf} = 0$, $\dot{p}^{Ff} = 0$, and the stress $\dot{\varepsilon}_{ii} = \beta_T \dot{T}$, then, equation (33) reduces to

$$\phi^{Mf}\beta_T\dot{T} = \zeta^{Mf}\beta_T\dot{T} + C_{24}\dot{T} \tag{37}$$

Therefore,

$$C_{24} = \left(\phi^{Mf} - \zeta^{Mf}\right)\beta_T \tag{38}$$

With the same steps, we could have

$$C_{34} = \left(\phi^{Ff} - \zeta^{Ff}\right)\beta_T \tag{39}$$

### 5.3 Governing equations

#### 5.3.1 Mechanical behaviour

Assuming the mechanical equilibrium condition $\partial\sigma_{ij}/\partial x_j = 0$, and using displacement variables $d_i\,(i=1,2,3)$ through $\varepsilon_{ij} = \frac{1}{2}\left(d_{i,j} + d_{j,i}\right)$, from stress equation (32) leads to

$$\underbrace{G\nabla^2\dot{\mathbf{d}} + \left(\frac{G}{1-2\theta}\right)\nabla\left(\nabla\cdot\dot{\mathbf{d}}\right)}_{1} - \underbrace{\zeta^{Mw}\nabla\dot{p}^{Mw} - \zeta^{Fw}\nabla\dot{p}^{Fw}}_{2} - \underbrace{K\beta_T\nabla\dot{T}}_{3} = 0 \tag{40}$$

in which $\theta$ is Poisson's ratio.

The physical meaning of terms in equation (40) are

1: Elastic deformation of the solids.

2: The hydro coupling term, describes the influence of both pore and fracture water pressure on the deformation of the solids.

3: The thermal coupling term, describes the influence of temperature change on the deformation of the solids.

#### 5.3.2 Hydraulic behaviour

From the fluid mass balance equation (4), density relationship (2) and Euler identity (19), the conservation equation of fluid can be written as

$$\dot{\upsilon}^{\beta}\rho_{\beta}^{\beta} + \upsilon^{\beta}\dot{\rho}_{\beta}^{\beta} + J\nabla\cdot(\rho_{\beta}^{\beta}\mathbf{u}^{\beta}) + J\tilde{\rho}^{\beta} = 0 \tag{41}$$

The fluid density is a function of pressure and temperature $\rho_\beta^\beta = \rho_\beta^\beta\left(p^\beta, T\right)$ (Hosking et al., 2020)

$$\dot{\rho}_\beta^\beta(T, p^\beta) = \rho_\beta^\beta\left(\frac{1}{K_\beta}\dot{p}^\beta - \beta_w \dot{T}\right) \tag{42}$$

in which $K_\beta = \frac{1}{\rho_\beta^\beta}\left(\frac{\partial \rho_\beta^\beta}{\partial p^\beta}\right)_T$ is the bulk modulus of the fluid, $\beta_\beta = -\frac{1}{\rho_\beta^\beta}\left(\frac{\partial \rho_\beta^\beta}{\partial T}\right)_{p^\beta}$ is the thermal expansion coefficient of the fluid.

Invoking equation (42) and (33)/(34) into equation (41), and neglecting the space variation of density (e.g. $\nabla \cdot \rho_\beta^\beta = 0$), assuming $J = 1$, the governing equation for the transport of matrix pore/fracture fluid can be obtained as

Matrix pore fluid:

$$\underbrace{\zeta^{Mf}\nabla\cdot\dot{\mathbf{d}} + Q\dot{p}^{Mf} + B\dot{p}^{Ff} + C_{24}\dot{T}}_{1} + \underbrace{\frac{\upsilon^{Mf}}{K_{Mf}}\dot{p}^{Mf} - \upsilon^{Mf}\beta_{Mf}\dot{T}}_{2} + \underbrace{\tilde{\rho}^{Mf}}_{3} = \underbrace{\frac{k^{Mf}}{\nu^{Mf}}\nabla^2 p^{Mf}}_{4} \tag{43}$$

Fracture fluid:

$$\underbrace{\zeta^{Ff}\nabla\cdot\dot{\mathbf{d}} + B\dot{p}^{Mf} + Z\dot{p}^{Ff} + C_{34}\dot{T}}_{5} + \underbrace{\frac{\upsilon^{Ff}}{K_{Ff}}\dot{p}^{Ff} - \upsilon^{Ff}\beta_{Ff}\dot{T}}_{6} + \underbrace{\tilde{\rho}^{Ff}}_{7} = \underbrace{\frac{k^{Ff}}{\nu^{Ff}}\nabla^2 p^{Ff}}_{8} \tag{44}$$

The physical meaning of terms in equation (43) and (44) are

1 and 5: Liquid variation caused by the porosity change, due to solid deformation, pore and fracture pressure change, and temperature change.

2 and 6: Liquid variation within the pore and fracture caused by liquid mass density change, due to the water pressure and temperature change.

3 and 7: Liquid variation caused by the exchange, due to the water pressure gradient between pore and fracture.

4 and 8: Convection term calculated by Darcy's Law.

The exchange term in equations (43) and (44) can be described by (Kazemi et al., 1976; Ranjbar and Hassanzadeh, 2011; Warren and Root, 1963)

$$\tilde{\rho}^{Mf} = -\tilde{\rho}^{Ff} = \frac{\chi k^{Mf}}{\mu^{f}}\left(p^{Mf} - p^{Ff}\right) \tag{45}$$

where $\chi$ is the shape factor, and it can be linked to the fracture spacing $L$ and the dimension of the porous matrix block $N$ ( $N = 1, 2, 3$ )(Warren and Root, 1963)

$$\chi = \frac{4N(N+2)}{L^2} \tag{46}$$

The fracture spacing is the average spacing between each parallel fracture. Sometimes a different fracture spacing or a different width may exist along each of the directions to simulate the proper degree of anisotropy.

### 5.3.3 Thermal transport

The balance equation for the heat of the mixture can be written as:

$$\left(q^{s} + \sum q^{\beta}\right)^{\cdot} + \left(q^{s} + \sum q^{\beta}\right)\nabla \cdot \mathbf{v}^{s} + \nabla \cdot \mathbf{q}' + \sum h^{\beta}\mathbf{I}^{\beta} = 0 \tag{47}$$

where $\sum h^{\beta}\mathbf{I}^{\beta}$ is the heat flow carried by fluid, using the relationship (14), and considering the expression $h^{\beta} = C^{\beta}T$, it can be linked to the fluid velocity through

$$h^{\beta}\mathbf{I}^{\beta} = C^{\beta}T\rho_{\beta}^{\beta}\mathbf{u}^{\beta} \tag{48}$$

$q^{s}$ and $q^{\beta}$ are the heat density of the solid and the fluid, they can be expressed in terms of specific heat capacity of the solid $C^{s}$ and the fluid $C^{\beta}$ through

$$q^{s} = \rho^{s}C^{s}T\,,\ q^{\beta} = \rho^{\beta}C^{\beta}T \tag{49}$$

Using the density relationship (2), Euler's formula (19) and equation (48), (15), and further assuming $J = 1$, equation (47) becomes

$$\underbrace{\left(\upsilon^{s}\rho_{s}^{s}C^{s}T + \sum \upsilon^{\beta}\rho_{\beta}^{\beta}C^{\beta}T\right)^{\cdot}}_{1} = \underbrace{\nabla \cdot \left(\lambda \nabla T\right)}_{2} - \underbrace{\sum C^{\beta}T\rho_{\beta}^{\beta}\nabla \cdot \mathbf{u}^{\beta}}_{3} \tag{50}$$

where $\upsilon^{s} = J - J\sum \phi^{\beta}$ is the volume fraction of the solid in the reference configuration.

The physical meaning of terms in equation (50) are

1: Heat density change over time. This term is influenced by both hydro and mechanical fields due to the fully coupled porosity change.

2: Thermal transport driven by the temperature difference (conduction).

3: Hydro coupling term, represents the heat transport driven by convection of the water flow.

If the porosity is considered as a constant value instead of a dynamic variable, equation (50) becomes

$$\left(\upsilon^s \rho_s^s C^s + \sum \upsilon^\beta \rho_\beta^\beta C^\beta\right)\dot{T} = \nabla \cdot \left(\lambda \nabla T\right) - \sum C^\beta T \rho_\beta^\beta \nabla \cdot \mathbf{u}^\beta \tag{51}$$

where $\left(\upsilon^s \rho_s^s C^s + \sum \upsilon^\beta \rho_\beta^\beta C^\beta\right)$ are treated as effective volumetric heat capacity.

Equation (51) is the basic and classic thermal transport equation, it is adopted by many researchers (Cui and Wong, 2021; Shi et al., 2019). However, it is obvious that equation (51) is not a fully coupled equation as it only includes the temperature influence but omits the strain (displacement) and pressure (matrix/fracture pressure) influence. Meanwhile, the porosity in equation (51) is a constant value, which is not consistent with real case as porosity changes with deformation, pressure and temperature. To develop the fully coupled thermal transport equation, the porosity in equation (50) is treated as a dynamic variable, then, the porosity dynamics equation (33) and (34) can be substituted into the derivative of equation (50). Following that, the heat transport equation can be derived as

$$\underbrace{\left[C^s \upsilon^s \rho_s^s + C^f \left(\upsilon^{Mf} + \upsilon^{Ff}\right)\rho_f^f\right]\dot{T}}_{1}$$
$$+\underbrace{\left(C^f \rho_f^f T - C^s \rho_s^s T\right)\left[\left(\zeta^{Mf} + \zeta^{Ff}\right)\nabla \cdot \dot{\mathbf{d}} + \left(Q + B\right)\dot{p}^{Mf} + \left(B + Z\right)\dot{p}^{Ff} + \left(C_{24} + C_{34}\right)\dot{T}\right]}_{2} = \tag{52}$$
$$\underbrace{\nabla \cdot \left(\lambda \nabla T\right)}_{3} - \underbrace{\sum C^\beta T \rho_\beta^\beta \nabla \cdot \mathbf{u}^\beta}_{4}$$

where $C^f$ and $C^s$ are treated as constant, and the assumption $\rho_{Mf}^{Mf} = \rho_{Ff}^{Ff} = \rho_f^f$ is used.

The second term in equation (52) is the newly introduced term, making our model different from most existing models. The physical meaning of this term is: The heat density change of the dual porosity media due to the porosity change (called porosity induced heat density change in this paper), which is determined by solid deformation, fluid pressure change and thermal expansion.

Equation (52) is the new developed heat transport equation for dual porosity media. It includes the deformation (mechanical), matrix pressure, fracture pressure (hydro) and temperature terms, making it a fully coupled equation. From the derivation steps, it can be found that the mechanical and hydro processes are coupled into the thermal equation through the porosity change. When the porosity change is not significant, usually equation (51) can be used to model the heat transport, but when porosity changes significantly, equation (52) is required.

### 5.4 Validation and limitations of the model

The mathematical model proposed in this research determines the coupling behaviour of solid deformation, fluid flow, and heat transfer in dual-porosity media. Since the experimental data of fully coupled THM behaviour in dual-porosity formation is very limited, the presented model is compared with existing models developed by other researchers for theoretical validation.

Compared with the model by Gelet et al. (2012b), which was derived through a thermodynamics approach, the model proposes the same set of mechanical and hydraulic constitutive equations but different thermal equation. The difference with the research done by Bai and Roegiers (1994) and Khalili and Selvadurai (2003) is that the presented model considered the fully coupled porosity change in all the thermal-hydro-mechanical equations. Masters et al. (2000) model has similar mechanical and thermal equations with the proposed model, while lacks the consideration of thermal and mechanical effects on fracture water flow. Another innovation is that the proposed model considers fully coupling effects of hydro and mechanical fields on the heat transfer, apart from the indirect effects by the convection, thermo-hydro-mechanical coupling also changes the heat density by directly affecting the porosity (the second term in equation (52)). The porosity change in heat density term was ignored in the model proposed by Shi et al. (2019) and Cui and Wong (2021). Salimzadeh et al. (2018) and Li et al. (2022a) considered the heat density change due to the course of the solid deformation and fluid pressure change; a new heat density change term which represents gas sorption was added (Li et al., 2022b), while all of them ignored the heat density change induced by the porosity change due to temperature.

The governing equation of hydro-mechanical coupling is consistent with models derived from the mechanics approach (Khalili, 2003; Khalili, 2008). The model can be degenerated to the classical Dual-Permeability Model by Simunek and van Genuchten (2008) if the mechanically

coupled effect and thermal transfer are ignored. The fluid exchange term is consistent with previous research (Khalili, 2003; Zhao and Chen, 2006). If the fracture and pore are viewed as continuums with no significant difference, the model can be simplified to classical THM models for porous media developed by Coussy (2004) and Magnenet et al. (2014).
The model derived in this study takes the HDR as two isotropic continuums (fracture and pore), which ignores the anisotropic transport in some of the fractured porous media. In addition, the chemical effect (precipitation and dissolution) is ignored in the model.

# 6 Coupled THM numerical model and simulation solution

In this section, a numerical model is built based on COMSOL software (Version 5.6) to study the fully coupled Thermo-Hydro-Mechanical behaviour in a dual-porosity HDR reservoir. Equation (52), together with equations (40), (43), (44), are adopted in the modelling.

Then a baseline model is built, for comparison with the proposed model. The baseline model uses the same conditions as the proposed model and adopts equation (51), together with equations (40), (43), (44), but ignores the porosity change in all equations to explore the effects of dynamic porosity on thermal production and also to demonstrate the innovations of the THM equations proposed in this paper.

## 6.1 Numerical model setup

As shown in Figure 1, a hot dry rock layer which is 1000 m long and 600 m wide is studied. To extract the thermal energy, an enhanced geothermal system was built in this reservoir, creating an artificial fracture network in the reservoir. A highly fractured block is selected to model the coupled THM behaviour during geothermal production. The block size is 600 m in length, 600 m in width and 200 m in thickness. The block is located 1800m below the surface and the injection well and production well are vertically located at the same elevation (middle depth of the block). Take the projected southwestern corner of the block on the ground as the origin, the coordinates of the injection well are located at (100, 300, -1900); the coordinates of the production well are (500, 300, -1900). The diameter of the wells is 0.1m and the length is 20m. The grey quadrilateral shows the cut plane (XZ plane) where the two wells are located, the black dash line shows the direction between the injection and production well along the X-axis.

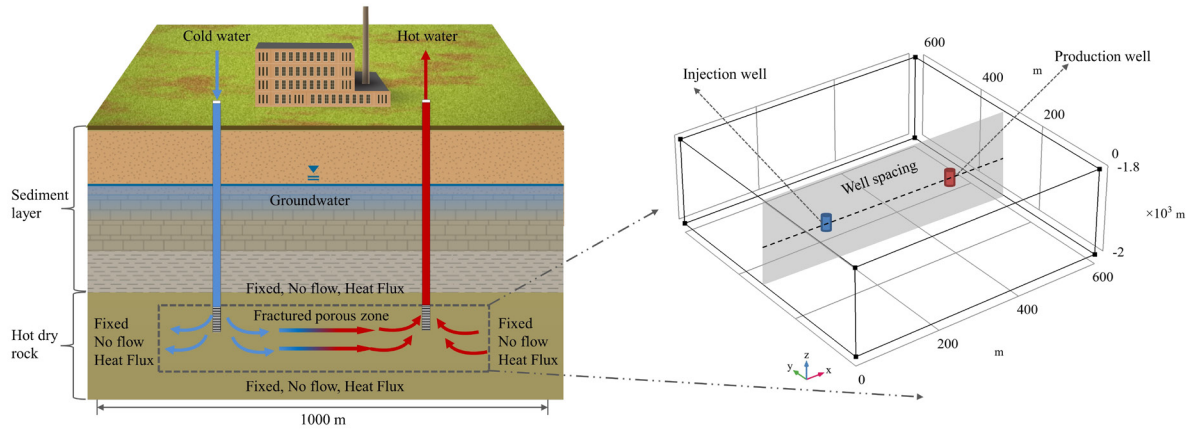


Fig. 1 Conceptual model of the enhanced geothermal system

For the mechanical boundary conditions, all six boundaries of the model are set as Fixed Constraint which means no displacement at each boundary. An equilibrium stage is assumed at the initial time in the full simulated domain because this study focuses on the coupling effects after the injection, the displacement of the rock at the beginning is 0.

For the hydraulic boundary conditions, it is assumed that the permeability of the surrounding rock is extremely low, No Flow is used for all six boundaries, which means that there is no water exchange across all the boundaries, consistent with previous research (Aliyu and Archer, 2021a). The water pressure of the production well is set to p_inj , and the value of p_inj was changed to represent different scenarios during the simulation. The water pressure of the production well is fixed at 10 MPa. The initial water pressure of the pore and fracture are the same (20 MPa).

For the thermal boundary conditions, all six boundaries are set as Heat Flux boundary, the heat supply by the reservoir outside the model domain is calculated using the temperature in the domain and outside the domain, as follows, $\mathbf{q}_0 = h\left(T_{out} - T\right)$, where $h$ is the heat transfer coefficient, $T_{out}$ is the temperature outside the domain (remains a fixed temperature same as the initial temperature in the simulated domain, along with the simulation), $T$ is the temperature in the modelled domain. The injection water temperature is set to T_inj, which was changed to investigate different scenarios. At the initial time, the temperature on the top boundary is 409.3 K while the temperature on the bottom boundary is 417.3 K, and the temperature distribution in the simulated domain is calculated from the natural temperature gradient (40K/km).

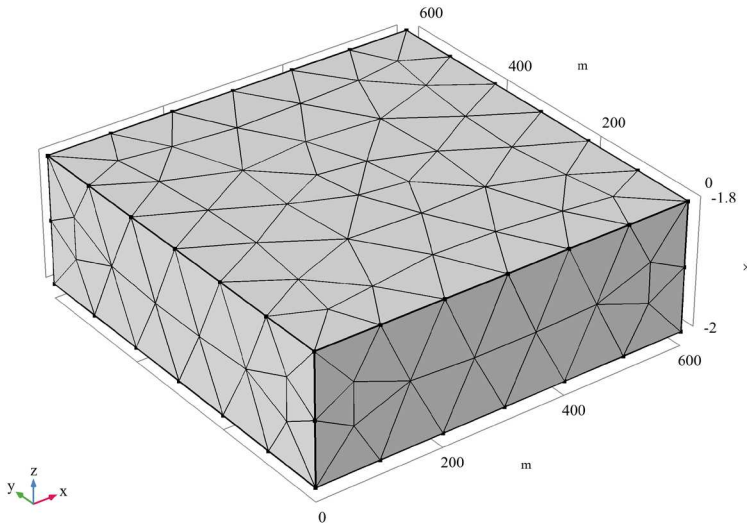


Fig. 2 Numerical mesh of the modelled block

The numerical mesh used in the model is shown in Fig. 2. The simulated domain was discretized using free tetrahedral, with 1977 total elements. Elements near the wells were refined to better study the high gradient of water pressure, each well was refined to 29 nodes.

The time step from the first year to the 100 year was 1 year, while the time step within 1 year was 0.01 year to ensure convergence due to relatively high water velocity in the early stage. A Newton nonlinear method with a constant damping factor is used for the equation solving in the numerical model. The maximum number of iterations was set as 1000, with a relative tolerance of 0.01.

The model parameters and basic settings are shown in Table 1. The parameters are referenced from Gelet et al. (2012a) and Abousleiman and Nguyen (2005). To explore the effects of different parameters on the production performance of the HDR system, different values for several parameters are used in the simulation to represent multiple scenarios.

Table 1 Model parameters and model setting

| Parameter | Value | Description |
|---|---|---|
| $E$ | $1.853\times10^{9}\,Pa$ | Young's modulus of total rock |
| $K_s$ | $27.5\times10^{9}\,Pa$ | Bulk modulus of solid grains |
| $K$ | $1.103\times10^{9}\,Pa$ | Bulk modulus of total rock |

| | | |
|---|---|---|
| $L$ * | 5 $m$ | Fracture spacing |
| $\phi_0^{Mf}$ | 0.15 | Initial porosity of porous |
| $\beta_s$ | $1.8\times10^{-5}\,K^{-1}$ | Solid thermal expansion coefficient |
| $k_0^{Ff}$ * | $1\times10^{-13}\,m^2$ | Fracture permeability |
| $k_0^{Mf}$ | $2\times10^{-16}\,m^2$ | Matrix permeability |
| $\phi_0^{Ff}$ | 0.015 | Initial porosity of fracture |
| $\theta$ | 0.22 | Poisson ratio |
| $K_f$ | $4.3\times10^{9}\,P$a | Compressibility of fluid |
| $K_{pb}$ | $1.226\times10^{9}\,P$a | Bulk modulus of porous block |
| p_inj * | 30 M$P$a | Water pressure of injection well |
| T_inj * | 293.15 K | Temperature of injection water |
| Time | 100 a | Total simulation time |

* This means the parameter is set to different values to test the product performance in the simulation (shown in section 6.3).

### 6.2 Temperature evolution and heat transfer in the HDR

Figure. 3 presents the temperature distribution along the XZ plane at different times using the basic parameters in table 1. The blue colour represents lower temperature while the red means higher temperature. At the initial time (Time=0a), due to the natural temperature gradient, the upper boundary holds the lowest temperature of 409.3K while the bottom boundary has the highest temperature of 417.3K. After the injection start, the cold water from the injection well transport to the production well via the porous matrix and the fractures, as a result, the temperature around the injection well started to decrease (T=0.05a, 1a); as time goes by, the temperature in the central part of the reservoir decreases heavily, surrounded by the relatively hot water at the lateral, vertical boundaries and the rightmost end of the rock (T=10a, 30a). Since the temperature at the boundaries became lower than the outside rock, the rock received heat energy from surrounding rocks via heat conduction.

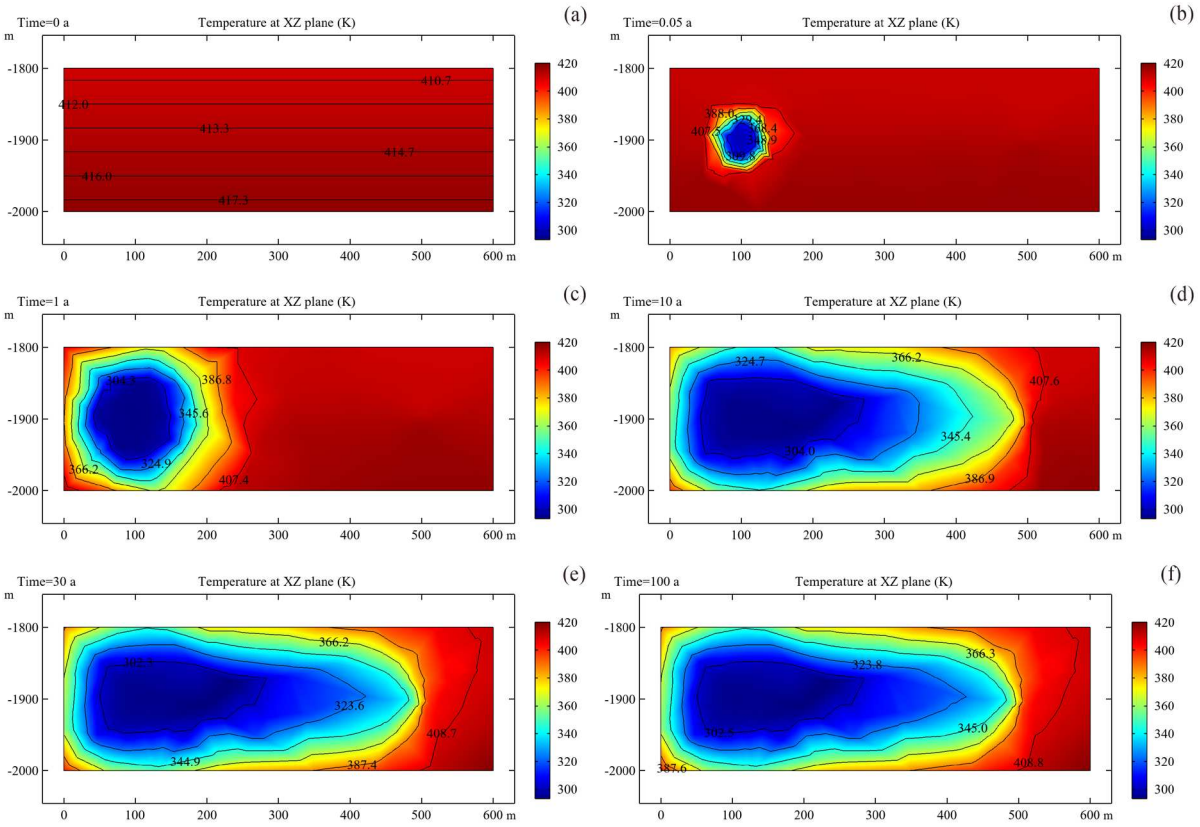


Fig. 3 Temperature and conductive heat evolution at XZ plane. The heat conduction follows the direction of temperature gradient inside the rock.

The direction of heat convection and 3D temperature slice after production are shown in Fig. 4. The arrow lines in this figure show the directions of the convective heat flux (heat flux carried by water), the direction of convective heat flux is the same as the direction of water flow. Along the convection path from the injection well to the production well, the water temperature gradually increases, since the cold water is heated by the solids and hot water in the host rock during this transport process. On the 3D view, the domain occupied by cold water is an ellipsoid, with the expansion of this ellipsoid, the temperature change became lower, from the injection well to the production well.

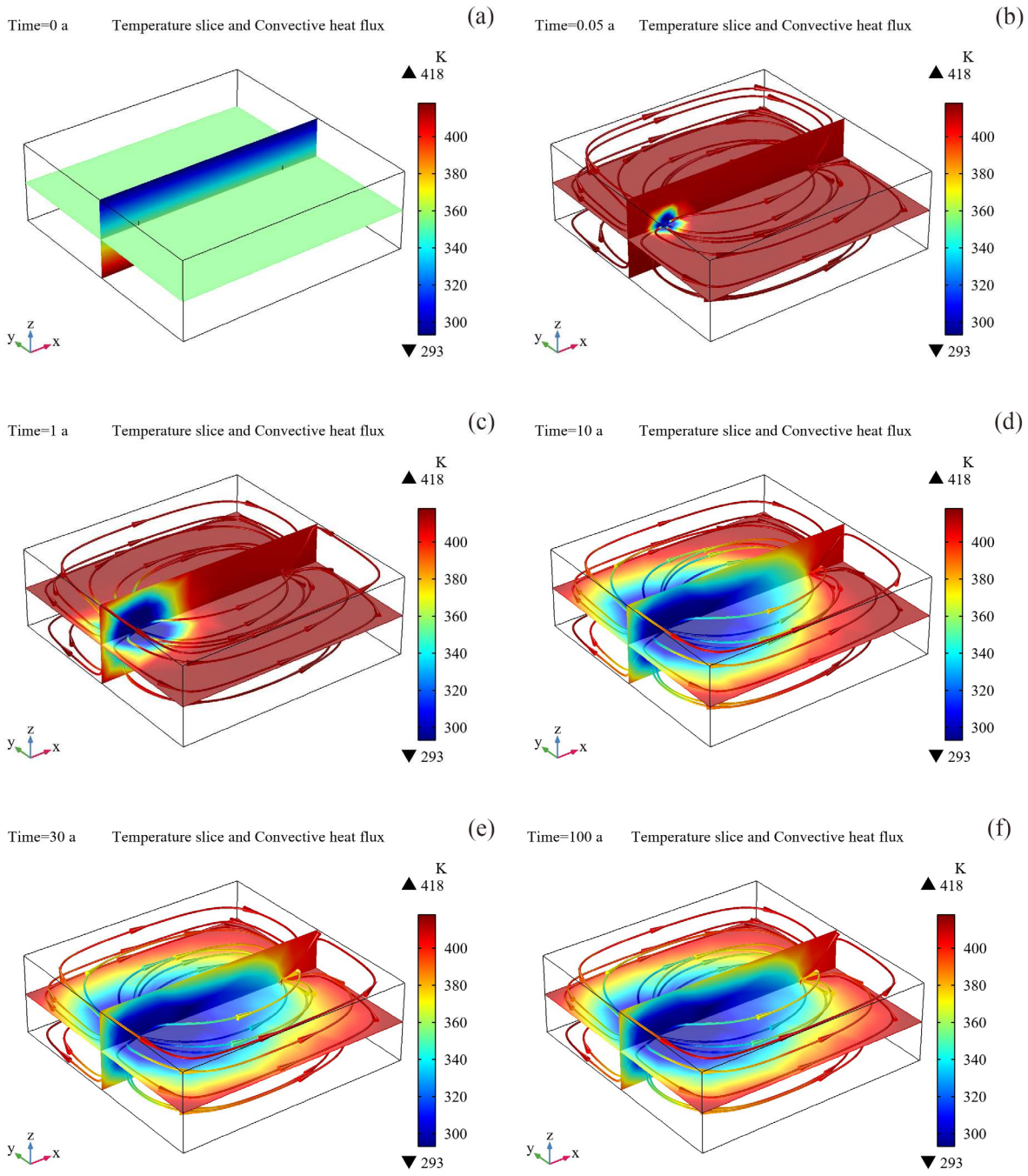


Fig. 4 3D Temperature slice on the XZ plane and YZ plane, together with the direction of heat convection in the rock.

### 6.3 Production temperature evolution

One of the most important performances in HDR is the production temperature. Several operative parameters (e.g., permeability, injection temperature, injection pressure, fracture spacing) can affect the coupled heat flow in the rock, hence controlling the temperature

distribution and energy production. Apart from the basic values of permeability, injection temperature, injection pressure, and fracture spacing listed in table 1, different values of these parameters are used to explore their influence on the production temperature, as shown in Fig. 4. From Fig. 5, all the production curves display a similar profile, the production temperature started to decrease after 2-10 years of stable stage. In the declining stage, the production temperature slowly reached about 380 K after 28 years. And finally, the production temperature reached a constant value and remained fixed, which means that the new heat equilibrium has been reached in the HDR. Unlike the results by Aliyu and Archer (2021b) and Sun et al. (2018), which use a thermal insulated boundary and obtained decreasing production temperature throughout the calculation period, this model uses a heat flux boundary which means a heat supply from surrounding rocks is permitted so that an equilibrium stage is possible during the production period.

The permeability seems to show the strongest effect on production temperature, while the influence of fracture spacing is so weak with the chosen parameters that it can be ignored in most of the production period except at the end of the declining stage. The initial stable stage is determined by the heat transfer speed. The production temperature started to decline till the outside heat supply cannot compensate for the heat loss around the production well, which is induced by heat convection and conduction. With the increase of permeability and the injection pressure, the heat convection became more intensive, so the length of the initial stable stage became shorter. For the standard scenario (black line), the production temperature reached the final equilibrium after 26 years with a temperature of about 380 K. While the time length became shorter in the scenario with high permeability or with high injection pressure, which also provides lower equilibrium temperature of production water since these scenarios mean higher injection water flux into the HDR. As shown in Fig 4.b, when the injection temperature is high, the production temperature takes a shorter time to reach the equilibrium (a higher temperature value), this is mainly due to such kind of scenario need less outside heat supply than the scenario with colder water injection before the final equilibrium. The variation of fracture spacing represents the fracturing level of the HDR, higher spacing means a weaker exchange between pore and fracture water, which results in a longer time length to final equilibrium.

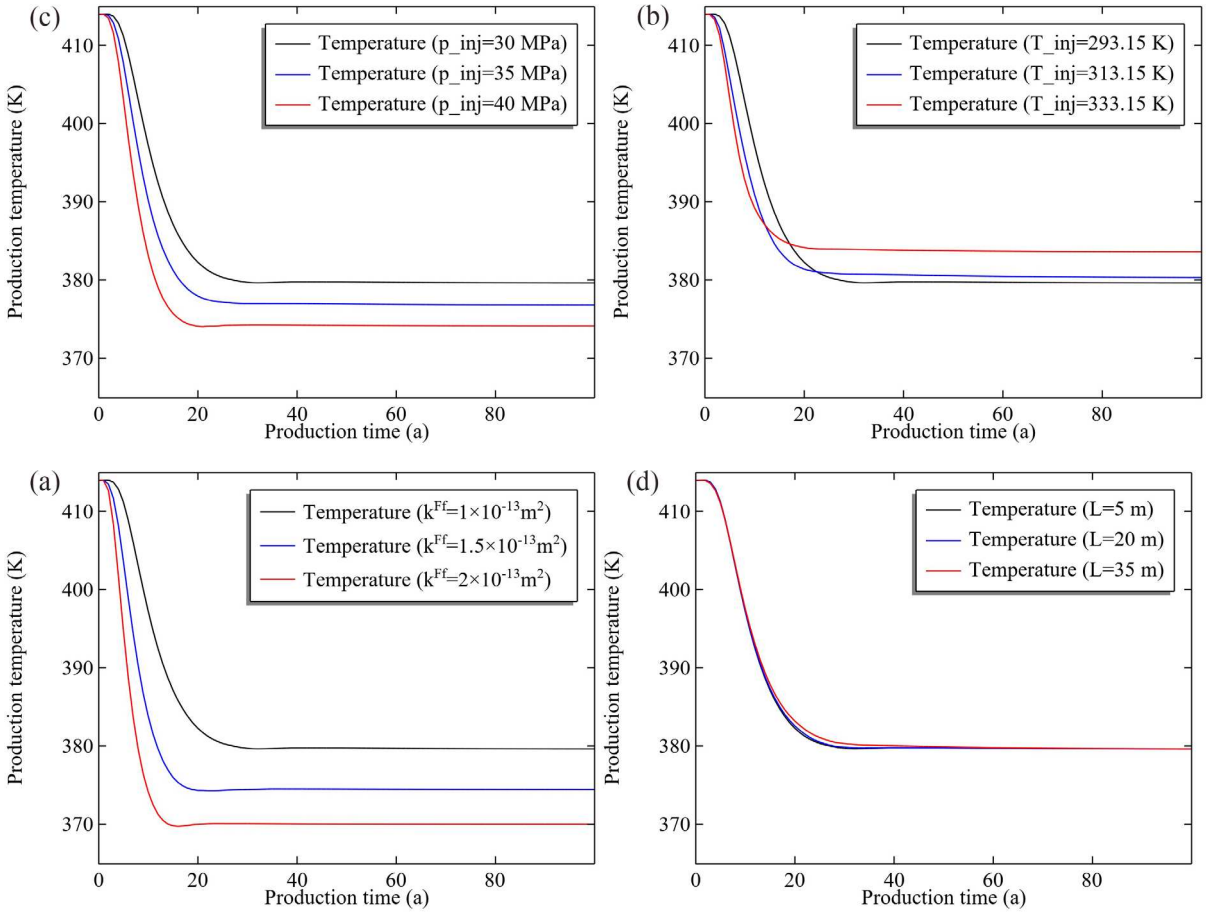


Fig. 5 Production temperature for the different cases, the black line represents the results using the parameters in table 1, the blue one and red one show the results using parameters of low and high values.

The location of wells also influences the production performance, which is consistent with previous research outcomes (Aliyu and Archer, 2021a; Shi et al., 2019). Figure 6 shows the curves of production temperature when the wells are located at depth of -1860m (high case), -1900m (middle case) and -1940m (low case). For the low and high cases, there are no stable stages in the early production. During early production, the production temperature is mainly determined by the rock temperature around the production well. Since the boundaries are no flow, when the well is located at a high position, the pumped water come from mostly the lower part, which leads to an increase in product temperature. In the contrast, the production temperature of low case experiences a quick decrease in the early stage.

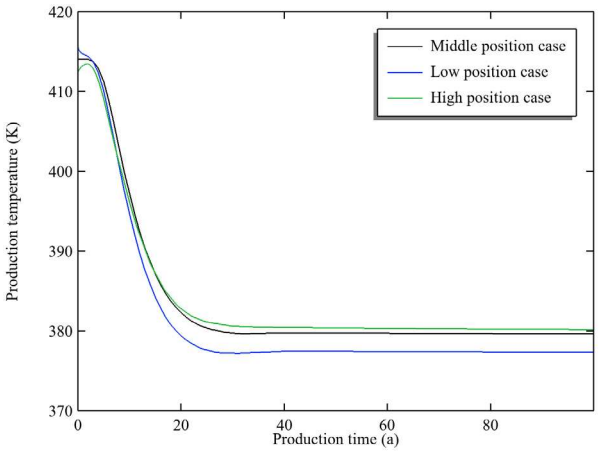


Fig. 6 Production temperature of different well depths

(well depth at -1860m for high case, -1900m for middle case and -1940m for low case)

### 6.4 Water pressure evolution and flow field in the HDR

Figure 7 shows the 3D flow field of pore and fracture water along the production period, which presents the pressure equilibrium surface and water flow direction. The different colours of surfaces and lines in the figures represent different pressure values and different flow speeds. The water pressures rapidly change at the very early stage of operation. The pressure around the injection well increases while the pressure around the production well decreases during the production period. After 0.05 years, the area where the pressure increase becomes much smaller while pressure in most of the rock becomes lower than the initial pressure (20 MPa). The pressure change in the fracture is much quicker than in the pore due to higher permeability, while the pressures become the same after a few weeks (indicating a relatively quick water exchange between pore and fracture). The flow map shows that the cold water flows from the injection well to the production well, and the water is heated by the rock and surrounding hot water during this process. Figure 7 shows that the Darcy's velocity in both pore and fracture gradually decreases with time, due to the decreased pressure gradient in the HDR. The fracture Darcy's velocity is almost three orders of magnitude larger than the pore Darcy's velocity.

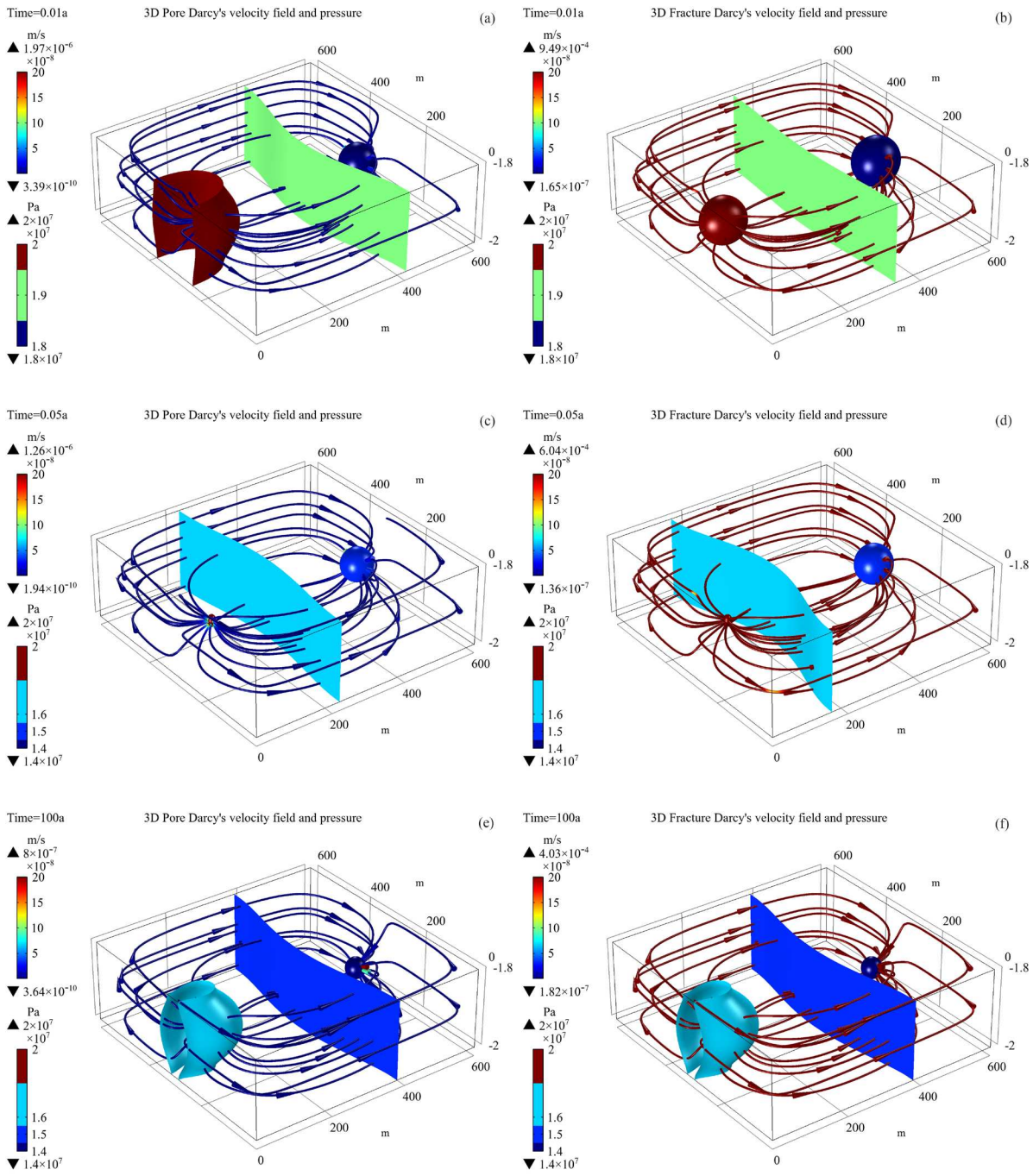


Fig. 7 3D Pore and fracture flow field at 0.01a, 0.05a and 100a in HDR. The coloured surfaces represent water pressure while the arrow lines represent the direction Darcy's velocity. The upper left colour legend in the figures show the and magnitude of Darcy's velocity.

### 6.5 Thermal and hydraulic effects on mechanical deformation

Figure 8 presents the displacement and temperature evolution in X direction along with the injection and production wells during the production period. As the pressure and temperature change, the reservoir experiences lasting deformation throughout the whole production time. Initially, temperature change only happened in a very small zone, the consolidation happens since the pressure decrease in most of the rock. The deformation magnitudes are lower near the vertical boundary due to a much slower change in water pressure. There is a peak value of consolidation around the injection well, which can attribute to the thermal stress by cold water (consistent with the intensive temperature change). After a few years, the low-temperature zone expands to the production well and finally reaches the right boundary. As a result, the peaks of the deformation keep moving towards the right boundary, it mainly appears in the area where the temperature gradient is high.

Noted that the previous section shows that the water pressure distribution tends to be stable at the later stage (after about 30 years), so the temperature change dominates the rock deformation after a few years while the fluid pressure change show influence mainly at the early stage.

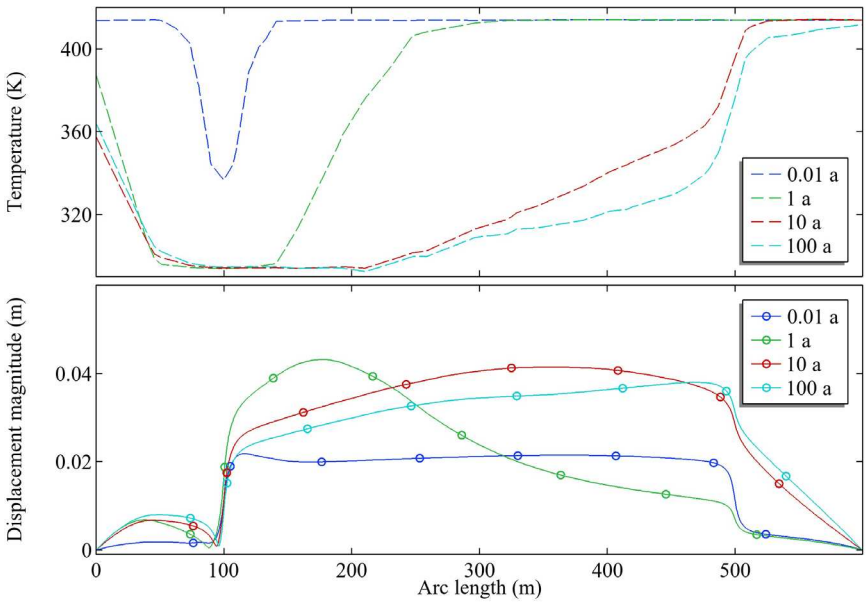


Fig. 8 Solid displacement (bottom) and temperature (top) change between injection and production well along the X direction

### 6.6 Multiphysics coupled porosity change

Figure 9 shows the evolution of the matrix pore porosity and fracture porosity during the production period. Due to the sharp change of pressure and temperature around the injection/production wells at the early stage (0.01 a), the porosity of both matrix pore and fracture near the injection/production wells changes sharply. As time goes by, almost all parts of the reservoir experience porosity change except the zones near the vertical boundary, since water pressure changes are very weak in these zones and there is very little temperature change due to the outside heat supply.

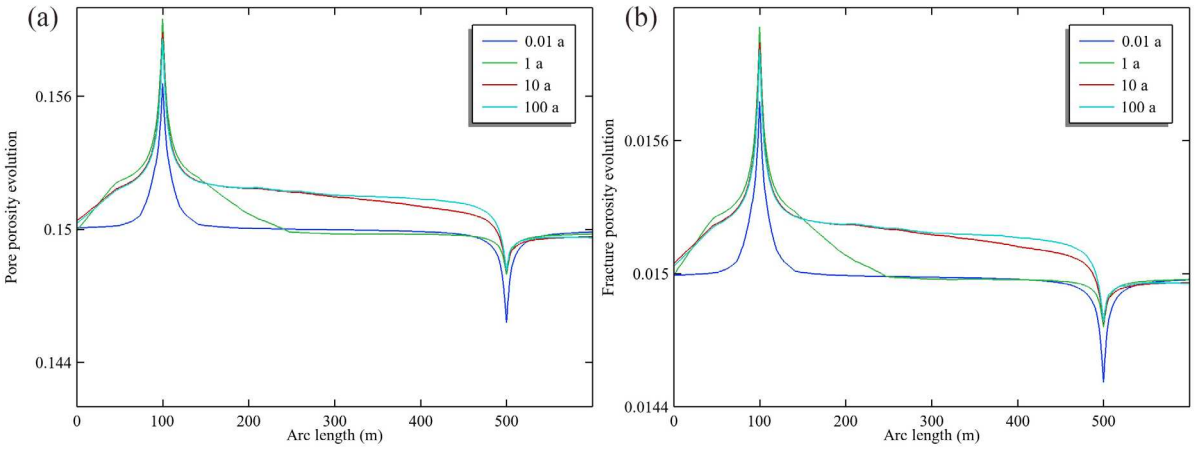


Fig. 9 Evolution of pore and fracture porosity between the injection and production well along the X direction

According to equation (33) (34), the porosity change is determined by strain, the fluid pressure of both pore and fracture, and the temperature. Figure 10 shows the porosity change induced by the three factors at the central point between the injection and production well.

The total porosity in both pore and fracture experiences a decrease at the very early stage, then increase to a steady value after a few years. The final porosity change of pore and fracture are about 0.00155 and 0.000185, accounting for 1.03% and 1.23%, respectively. Since the temperature in the HDR decrease till the equilibrium is established, the porosity change induced by temperature remains positive and accounts for the highest percentage of the total porosity change (more than 87%). The porosity change induced by fluid pressure remains negative along the production period since the pressure decrease till reaches its equilibrium value after about 30 years. The porosity change induced by solid deformation is negative at the beginning when the decreasing rate of water pressure is relatively high, which means the water pressure change

affects the solid deformation more than the temperature change does. After a few years, the porosity change induced by solid deformation becomes positive. The figure indicates that different behaviour dominates the porosity change at a different stages, the water pressure change is more important at the very early stage before the temperature change shows its dominant influence after a few years.

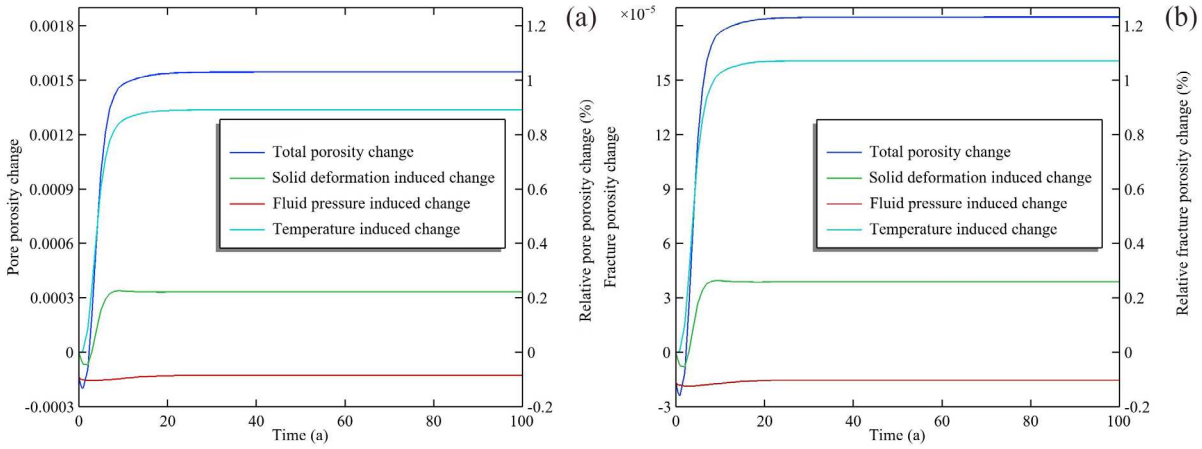


Fig. 10 Evolution of pore and fracture porosity at the central point between injection and production well

### 6.7 Comparison of the proposed model with the baseline model

The calculated results by the proposed model are compared with a baseline model to explore the key advance of the new model. Since equation (51) is the basic and classic thermal transport equation adopted by many researchers, it, together with equations (40), (43), (44), is selected as the baseline THM model. While equation (51) takes the porosity as constant value, to explore the influence of dynamic porosity, the proposed thermal equation (52) is reduced to the same form as equation (51) by eliminating the second term (porosity induced heat density change) but keeping the porosities as variables described in equations (33) and (34). Finally, the calculated result of the purposed model (using equation (52)) is compared to explore the influence of the porosity induced heat density change.

The production temperature of the baseline model and the proposed model are shown in Figure 11. The difference between the baseline model and the proposed model increase with time, before reaching its peak after 25 years with 3.26 K (accounting for 0.8 % of the production temperature). Then the difference finally decreases to about 1.2 K at the end (after 100 years). This difference is mainly due to the different permeability, higher permeability leads to a lower production temperature, which is consistent with the results of (Li et al., 2021). Since during the production period, the increase of porosity leads to a higher permeability as well as a higher

flow rate of cold water, all these facts contribute to a shorter time length to the equilibrium and a lower equilibrium temperature. The baseline model ignores the dynamic porosity, which leads to an overestimate of production temperature along the production time.

The effects of porosity induced heat density change on heat transfer can be determined from the comparison of the red line with the blue line. Note that if the porosity induced heat density change is ignored, this leads to a very small difference, with the largest difference of 0.25 K (accounting for 0.061 % of the production temperature) within the first 3 years.

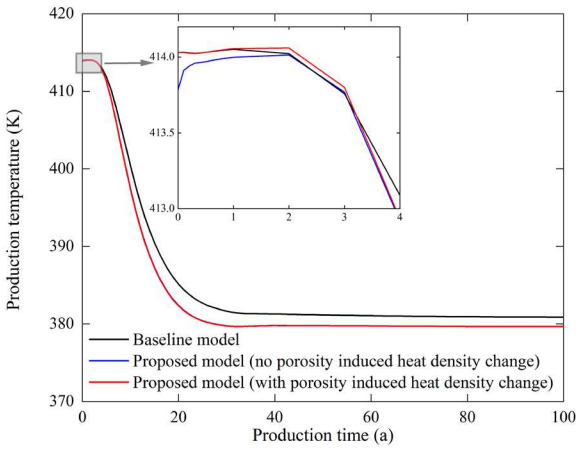


Fig. 11 Production temperature evolution calculated by baseline model (without considering dynamic porosity) and proposed model (red line considers porosity induced heat density change while blue line doesn't)

Figure 12 shows the evolution of porosity induced heat density change due to different factors (i.e., solid deformation, fluid pressure and temperature) with time. Similar to the porosity change evolution, the fluid pressure dominates the total porosity induced heat density change at the very initial stage before increasing to about 0 later, since the fluid pressure keeps decreasing. The solid deformation part is negative at the initial stage since the consolidation happens, then becomes positive due to thermal shrinkage. After the initial stage, the temperature change contributes to a major part of the total porosity induced heat density change, which accounts for more than 85% after 7 years. This indicates that ignoring the porosity induced heat density change due to temperature may lead to significant difference at long-term calculation (e.g., after 20 years, 30 years) since the temperature change in a rock is much slower than the change of solid deformation and fluid pressure. Noted that although the porosity induced heat density change doesn't lead to considerable errors in production temperature results in this paper, it may show important influences in some field cases where water pressure

and temperature change significantly or rapidly and some field cases subject to complex in-situ stress condition.

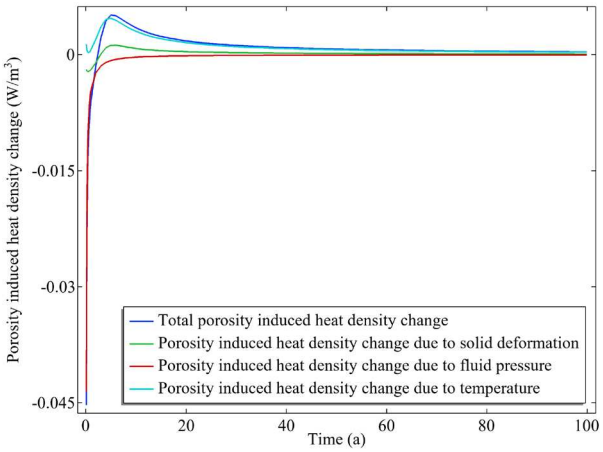


Fig. 12 Evolution of porosity induced heat density change at the central point between injection and production well

# 7 Conclusion

This paper develops a mathematical model for thermo-hydro-mechanical coupled behaviour in dual-porosity media using the Mixture-Coupling theory, which is based on non-equilibrium thermodynamics and mixture theory. The constitutive model linking different physical phenomena in the dual-porosity media is obtained based on the analysis of Helmholtz free energy change. The final governing equation is presented based on further assumptions of elastic and isotropic conditions. The proposed equations show potential advantages in studying the fully coupling effects of hydro and mechanical fields on heat transfer, by theoretically comparing with other research.

A numerical simulation is performed to investigate the potential application of the presented model on the EGS and to compare it with the baseline model. The simulation provides results of the thermal, hydro, and mechanical behaviour during the production of EGS. The analysis reveals that the coupling effects of thermo-hydro-mechanical fields in dual-porosity media determine the performance of EGS. The production temperature remains stable at the early stage (2-10 years), then the production temperature reached about 380 K after 28 years and keeps constant throughout the whole production. The maximum porosity change of pore and fracture are about 0.00155 and 0.000185, accounting for 1.03% and 1.23%, separately. The porosity change is dominated by thermal effects (accounting for more than 87% of the total porosity change). Specifically, the baseline model which ignores dynamic porosity

overestimates the production temperature by about 3.26 K after 25 years, while the proposed model can improve the calculation performance, especially for long-term prediction (reducing up to 0.8 % relative error on temperature prediction in this case).

This study explores the thermo-hydro-mechanical coupling in dual-porosity media using constitutive and numerical model, and may help the exploration, planning and production management of the geothermal reservoir.

## CRediT authorship contribution statement

**Kai WANG:** Methodology, Software, Writing – original draft. **Jiahui ZHOU:** Methodology, Writing – Original Draft, Writing – review & editing. **Yue MA:** Conceptualization, Methodology, Writing – Original Draft; **Aizhong DING:** Supervision; **Xiaohui CHEN:** Supervision

## Declaration of competing interest

The authors declare that they have no known competing financial interests or personal relationships that could have appeared to influence the work reported in this paper.

## Acknowledgement

The first and fourth authors would like to thank the National Key R&D Program of China (No.2019YFC1805503), National Key R&D Program of China (No.2018YFC1800905), the Key science and technology projects of Inner Mongolia autonomous region (2019ZD001).

### References

Abousleiman, Y., Nguyen, V., 2005. Poromechanics Response of Inclined Wellbore Geometry in Fractured Porous Media. Journal of Engineering Mechanics-asce - J ENG MECH-ASCE, 131. DOI:https://doi.org/10.1061/(ASCE)0733-9399(2005)131:11(1170)

Aifantis, E., 1980. On the problem of diffusion in solids. Acta Mechanica, 37(3-4): 265-296.

Aliyu, M.D., Archer, R.A., 2021a. Numerical simulation of multifracture HDR geothermal reservoirs. Renewable Energy, 164: 541-555. DOI:10.1016/j.renene.2020.09.085

Aliyu, M.D., Archer, R.A., 2021b. A thermo-hydro-mechanical model of a hot dry rock geothermal reservoir. Renewable Energy, 176: 475-493.

Aliyu, M.D., Chen, H.-P., 2017. Optimum control parameters and long-term productivity of geothermal reservoirs using coupled thermo-hydraulic process modelling. Renewable Energy, 112: 151-165.

Bai, M., Roegiers, J.-C., 1994. Fluid flow and heat flow in deformable fractured porous media. Int J Eng Sci, 32(10): 1615-1633.
Barenblatt, G.I., Zheltov, I.P., Kochina, I.N., 1960. Basic concepts in the theory of seepage of homogeneous liquids in fissured rocks [strata]. Journal of Applied Mathematics and Mechanics, 24(5): 1286-1303. DOI:10.1016/0021-8928(60)90107-6
Berryman, J.G., Wang, H.F., 1995. The elastic coefficients of double-porosity models for fluid transport in jointed rock. Journal of Geophysical Research: Solid Earth, 100(B12): 24611-24627.
Biot, M.A., 1956. Theory of Propagation of Elastic Waves in a Fluid-Saturated Porous Solid. II. Higher Frequency Range. The Journal of the Acoustical Society of America, 28(2): 179-191. DOI:10.1121/1.1908241
Chen, J., Jiang, F., 2015. Designing multi-well layout for enhanced geothermal system to better exploit hot dry rock geothermal energy. Renewable Energy, 74: 37-48. DOI:https://doi.org/10.1016/j.renene.2014.07.056
Chen, L., Voss, C.I., Fortier, D., McKenzie, J.M., 2021a. Surface energy balance of sub-Arctic roads with varying snow regimes and properties in permafrost regions. Permafrost and Periglacial Processes, 32(4): 681-701. DOI:https://doi.org/10.1002/ppp.2129
Chen, L., Yu, W., Lu, Y., Wu, P., Han, F., 2021b. Characteristics of heat fluxes of an oil pipeline armed with thermosyphons in permafrost regions. Applied Thermal Engineering, 190: 116694. DOI:https://doi.org/10.1016/j.applthermaleng.2021.116694
Chen, X., Pao, W., Thornton, S., Small, J., 2016. Unsaturated hydro-mechanical–chemical constitutive coupled model based on mixture coupling theory: Hydration swelling and chemical osmosis. International Journal of Engineering Science, 104: 97-109. DOI:https://doi.org/10.1016/j.ijengsci.2016.04.010
Coussy, O., 2004. Poromechanics. John Wiley & Sons.
Cui, X., Wong, L.N.Y., 2021. A 3D thermo-hydro-mechanical coupling model for enhanced geothermal systems. International Journal of Rock Mechanics and Mining Sciences, 143. DOI:10.1016/j.ijrmms.2021.104744
Dahash, A., Ochs, F., Giuliani, G., Tosatto, A., 2021. Understanding the interaction between groundwater and large-scale underground hot-water tanks and pits. Sustainable Cities and Society, 71: 102928. DOI:https://doi.org/10.1016/j.scs.2021.102928
Dykhuizen, R.C., 1990. A new coupling term for dual-porosity models. Water Resources Research, 26(2): 351-356. DOI:https://doi.org/10.1029/WR026i002p00351
Gelet, R., Loret, B., Khalili, N., 2012a. Borehole stability analysis in a thermoporoelastic dual-porosity medium. International Journal of Rock Mechanics and Mining Sciences, 50: 65-76. DOI:https://doi.org/10.1016/j.ijrmms.2011.12.003
Gelet, R., Loret, B., Khalili, N., 2012b. A thermo-hydro-mechanical coupled model in local thermal non-equilibrium for fractured HDR reservoir with double porosity. Journal of Geophysical Research: Solid Earth, 117(B7).
Heidug, W., Wong, S.W., 1996. Hydration swelling of water-absorbing rocks: a constitutive model. Int J Numer Anal Methods Geomech, 20(6): 403-430.
Hosking, L.J., Chen, M., Thomas, H.R., 2020. Numerical analysis of dual porosity coupled thermo-hydro-mechanical behaviour during CO2 sequestration in coal. International Journal of Rock Mechanics and Mining Sciences, 135. DOI:10.1016/j.ijrmms.2020.104473
Houhou, R., Laloui, L., 2022. Geomechanics for energy and the environment: Current developments. Geomechanics for Energy and the Environment: 100345.

Jiang, J., Younis, R.M., 2017. An Improved Projection-based Embedded Discrete Fracture Model (pEDFM) for Multiphase Flow in Fractured Reservoirs. Advances in Water Resources, 109. DOI:10.1016/j.advwatres.2017.09.017

Katchalsky, A., Curran, P.F., 1965. Nonequilibrium thermodynamics in biophysics. Harvard University Press, Cambridge, MA.

Kazemi, H., Merrill Jr, L., Porterfield, K., Zeman, P., 1976. Numerical simulation of water-oil flow in naturally fractured reservoirs. Society of Petroleum Engineers Journal, 16(06): 317-326.

Khalili, N., 2003. Coupling effects in double porosity media with deformable matrix. Geophysical Research Letters, 30(22). DOI:https://doi.org/10.1029/2003gl018544

Khalili, N., 2008. Two-phase fluid flow through fractured porous media with deformable matrix: TWO-PHASE FLUID FLOW THROUGH FRACTURED POROUS MEDIA. Water resources research, 44(5). DOI:10.1029/2007WR006555

Khalili, N., Selvadurai, A., 2003. A fully coupled constitutive model for thermo-hydro-mechanical analysis in elastic media with double porosity. Geophysical Research Letters, 30(24).

Lee, S.H., Lough, M.F., Jensen, C.L., 2001. Hierarchical modeling of flow in naturally fractured formations with multiple length scales. Water Resources Research, 37(3): 443–455. DOI:10.1029/2000WR900340

Leij, F.J., Toride, N., Field, M.S., Sciortino, A., 2012. Solute transport in dual-permeability porous media. Water Resources Research, 48. DOI:https://doi.org/10.1029/2011wr011502

Li, P. et al., 2022a. Fully coupled thermo-hydro-mechanical modeling and simulation of a fluid-saturated porous medium under local thermal non-equilibrium condition. International Journal of Heat and Mass Transfer, 195: 123195. DOI:https://doi.org/10.1016/j.ijheatmasstransfer.2022.123195

Li, T. et al., 2021. Modeling study of the thermal-hydraulic-mechanical coupling process for EGS based on the framework of EDFM and XFEM. Geothermics, 89: 101953.

Li, W. et al., 2018. Effect of local thermal non-equilibrium on thermoporoelastic response of a borehole in dual-porosity media. Applied Thermal Engineering, 142: 166-183.

Li, W. et al., 2022b. A fully coupled multidomain and multiphysics model considering stimulation patterns and thermal effects for evaluation of coalbed methane (CBM) extraction. Journal of Petroleum Science and Engineering, 214: 110506. DOI:https://doi.org/10.1016/j.petrol.2022.110506

Li, Z., Su, G., Zheng, Q., Nguyen, T.S., 2020. A dual-porosity model for the study of chemical effects on the swelling behaviour of MX-80 bentonite. Acta Geotechnica, 15(3): 635-653. DOI:10.1007/s11440-019-00762-5

Ma, Y., Chen, X., Hosking, L.J., Yu, H.-S., Thomas, H.R., 2022. THMC constitutive model for membrane geomaterials based on Mixture Coupling Theory. Int J Eng Sci, 171: 103605.

Magnenet, V., Fond, C., Genter, A., Schmittbuhl, J., 2014. Two-dimensional THM modelling of the large scale natural hydrothermal circulation at Soultz-sous-Forêts. Geothermal Energy, 2(1): 1-21.

Masters, I., Pao, W.K., Lewis, R., 2000. Coupling temperature to a double-porosity model of deformable porous media. International journal for numerical methods in engineering, 49(3): 421-438.

Ranjbar, E., Hassanzadeh, H., 2011. Matrix–fracture transfer shape factor for modeling flow of a compressible fluid in dual-porosity media. Advances in Water Resources, 34(5): 627-639.

Rutqvist, J. et al., 2009. A comparative simulation study of coupled THM processes and their effect on fractured rock permeability around nuclear waste repositories. Environmental Geology, 57(6): 1347-1360.
Saevik, P.N., Berre, I., Jakobsen, M., Lien, M., 2013. A 3D Computational Study of Effective Medium Methods Applied to Fractured Media. Transport in Porous Media, 100(1): 115-142.
Salimzadeh, S., Paluszny, A., Nick, H.M., Zimmerman, R.W., 2018. A three-dimensional coupled thermo-hydro-mechanical model for deformable fractured geothermal systems. Geothermics, 71: 212-224. DOI:10.1016/j.geothermics.2017.09.012
Shi, Y. et al., 2019. Numerical investigation on heat extraction performance of a multilateral-well enhanced geothermal system with a discrete fracture network. Fuel, 244: 207-226. DOI:10.1016/j.fuel.2019.01.164
Shu, Z., 1999. A dual-porosity model for two-phase flow in deforming porous media. Ph.D. Thesis, OK: The University of Oklahoma, Ann Arbor, 185 pp.
Simunek, J., van Genuchten, M.T., 2008. Modeling nonequilibrium flow and transport processes using HYDRUS. Vadose zone journal, 7(2): 782-797. DOI:10.2136/vzj2007.0074
Sun, Z.-x. et al., 2017. Numerical simulation of the heat extraction in EGS with thermal-hydraulic-mechanical coupling method based on discrete fractures model. Energy, 120: 20-33.
Sun, Z. et al., 2018. Numerical investigation on the heat extraction capacity of dual horizontal wells in enhanced geothermal systems based on the 3-D THM model. Energies, 11(2): 280.
Taron, J., Elsworth, D., 2009. Thermal–hydrologic–mechanical–chemical processes in the evolution of engineered geothermal reservoirs. International Journal of Rock Mechanics and Mining Sciences, 46(5): 855-864.
Tester, J.W. et al., 2007. Impact of enhanced geothermal systems on US energy supply in the twenty-first century. Philos Trans A Math Phys Eng Sci, 365(1853): 1057-94. DOI:10.1098/rsta.2006.1964
Wang, K., Ma, Y., Howlett, P.R., Ding, A., Chen, X.-H., 2022. New Unsaturated Dynamic Porosity Hydromechanical Coupled Model and Experimental Validation. International Journal of Geomechanics, 22(10): 04022171. DOI:doi:10.1061/(ASCE)GM.1943-5622.0002545
Wang, Y. et al., 2021. Major contribution to carbon neutrality by China's geosciences and geological technologies. China Geology, 4(2): 329-352. DOI:10.31035/cg2021037
Warren, J., Root, P.J., 1963. The behavior of naturally fractured reservoirs. Society of Petroleum Engineers Journal, 3(03): 245-255.
Wriggers, P., 2008. Nonlinear finite element methods. Springer Science & Business Media.
Zhang, G., Cui, B., 2011. The study of Thermal-Hydrologic-Mechanical (THM) coupled process in dual-porosity rock. Rock Mechanics: Achievements and Ambitions: 413.
Zhao, Y., Chen, M., 2006. Fully coupled dual-porosity model for anisotropic formations. International Journal of Rock Mechanics and Mining Sciences, 43(7): 1128-1133. DOI:https://doi.org/10.1016/j.ijrmms.2006.03.001
Zhao, Y., Feng, Z., Feng, Z., Yang, D., Liang, W., 2015. THM (Thermo-hydro-mechanical) coupled mathematical model of fractured media and numerical simulation of a 3D enhanced geothermal system at 573 K and buried depth 6000–7000 M. Energy, 82: 193-205.
Zhou, X., Gao, Q., Chen, X., Yu, M., Zhao, X., 2013. Numerically simulating the thermal behaviors in groundwater wells of groundwater heat pump. Energy, 61: 240-247. DOI:https://doi.org/10.1016/j.energy.2013.09.020